ChinaRxiv

AI translation · View original & related papers at
chinarxiv.org/items/chinaxiv-201611.00271

Microstructural Characterization of Dissimilar Metal Welded Joints in Nozzle Safe-Ends of Third-Generation Nuclear Power Plants: Post-Print

Authors: Ding Jie, Zhang Zhiming, Wang Jianqiu, Han Enhou, Tang Weibao, Zhang Maolong, Sun Zhiyuan

Date: 2016-11-04T00:00:00+00:00

Abstract

Utilizing microscopic analysis techniques including metallographic microscopy, transmission electron microscopy (TEM), scanning electron microscopy (SEM), microhardness testing, atomic force microscopy (AFM), magnetic force microscopy (MFM), and scanning Kelvin probe force microscopy (SKPFM), the metallographic microstructure, microhardness, distribution of major alloying elements, grain boundary types, and residual strain of the dissimilar metal welding joint A508/52M/316L at the safe end of the reactor pressure vessel in advanced pressurized water reactor nuclear power plants were analyzed, and the microstructure and properties across different thicknesses of the entire welding joint were compared. The research results indicate that there is no significant difference in microstructure and hardness along the weld depth direction. A layer of fine equiaxed grains formed by dynamic recrystallization appears at the bottom welding position. The residual strain in the heat-affected zone (HAZ) of the 316L base material is higher than in other locations of the welded component. The vicinity of the fusion line exhibits complex distributions of microstructure, microhardness, grain boundary types, elemental composition, and residual strain. TEM and MFM analyses reveal that there are granular precipitates enriched in Cr and Mo elements within the 316L base material matrix. SKPFM results demonstrate that these precipitates possess a more negative Volta potential than the matrix, rendering them less corrosion-resistant. The formation mechanism of the precipitates and their influence on the corrosion resistance of the safe end, particularly regarding stress corrosion cracking (SCC) susceptibility, require further investigation.

ChinaRxiv 中X

Full Text

Micro-Characterization of Dissimilar Metal Weld Joint for Connecting Pipe-Nozzle to Safe-End in Generation III Nuclear Power Plant

DING Jie[1], ZHANG Zhiming[1], WANG Jianqiu[1], HAN En-Hou[1], TANG Weibao[2], ZHANG Maolong[2], SUN Zhiyuan[2]

[1]Key Laboratory of Nuclear Materials and Safety Assessment, Chinese Academy of Sciences, Institute of Metal Research, Shenyang 110016, China
[2]Shanghai Electric Nuclear Power Equipment Co. Ltd., Shanghai 201306, China
Correspondent: WANG Jianqiu, Tel: (024)23893723, E-mail: wangjianqiu@imr.ac.cn

Supported by National Basic Research Program of China (No. G2011CB610502) and National Natural Science Foundation of China (No. 51025104)

Manuscript received 2014-06-06, in revised form 2014-10-12

Abstract

The dissimilar metal weld joint (DMWJ) in the primary water system of pressurized water reactors (PWRs) has proven to be a vulnerable component due to its susceptibility to various types of flaws. Thus, maintaining the integrity of such joints in the presence of defects is of great importance for the design and safe management of nuclear power plants (NPPs). For reliable integrity analysis of DMWJs, it is essential to understand the microscopic characteristics in all regions of the joint. In this work, optical microscopy (OM), transmission electron microscopy (TEM), scanning electron microscopy (SEM), microhardness testing, atomic force microscopy (AFM), magnetic force microscopy (MFM), and scanning Kelvin probe force microscopy (SKPFM) were utilized to investigate the microstructure, microhardness, distribution of main alloying elements, grain boundary characteristics, and residual strain in the A508/52M/316L DMWJ used for connecting the pipe safe-end to the reactor pressure vessel nozzle in PWRs. A comparative analysis of the microstructure and properties along the thickness direction of the DMWJ was also performed. The results showed that no region differed dramatically from other parts of the weldment in terms of microstructure and microhardness. A layer of fine grains resulting from unmelted filler metal was found in the backing weld region. The residual strain in the heat-affected zone (HAZ) of 316L was higher than in other regions. Meanwhile, drastic variations in microstructure, chemical composition distribution, and grain boundary character distribution (GBCD) were observed in both the 316L/52Mw and 52Mb/A508 interface regions. TEM and MFM analyses revealed numerous Cr- and Mo-rich precipitate particles distributed both along

grain boundaries and within grains in the 316L base metal, which were identified as precipitates with complex elemental composition rather than the typical stringer delta ferrite in 316L austenitic stainless steel. SKPFM results indicated that these precipitates have a more negative Volta potential than the matrix, making them more susceptible to corrosion. Therefore, further investigation into the formation mechanism of these precipitates and their impact on corrosion resistance, particularly stress corrosion cracking (SCC) sensitivity, is needed.

Keywords: dissimilar metal welding, microstructure, micro-hardness, chemical composition distribution, grain boundary character, residual strain

1. Introduction

Dissimilar metal weld joints (DMWJs) in PWR nuclear power plants are susceptible components in the primary coolant system, with main damage and failure modes including stress corrosion cracking (SCC), fatigue cracking, corrosion cracking, hot cracking, and lack-of-fusion defects. The formation of these defects is related to factors such as mechanical property variations along the weld joint, differences in thermal expansion coefficients and alloy elements between materials, welding residual stress, carbon migration, and service environment [1~10]. Over the past several decades, numerous cracking and leakage incidents in reactor primary loop piping safe-ends have been reported at nuclear power plants worldwide [1,2], making the integrity of this joint a critical prerequisite for safe NPP operation. Previous studies [3~7] have shown that alloy element diffusion near the fusion boundary, differences in crystal structure between weld and base materials, and welding heat flow lead to gradient changes in microstructure, microhardness, grain boundary character, and residual stress distribution in this region, which subsequently affect the mechanical properties and corrosion resistance of the entire weld joint, particularly SCC susceptibility. The narrow region adjacent to the fusion line exhibits higher SCC sensitivity than both the base metal and weld metal. Therefore, detailed micro-characterization of this DMWJ, especially the fusion line region, is essential for understanding its safety and stability in PWR primary water service environments.

Generation III PWRs mainly include AP1000 and EPR designs, with China developing CAP1000 and CAP1400 based on AP1000. The AP1000 NPP, developed by Westinghouse, is the design selected for most NPPs under construction or planned in China. The filler metal used for safe-end welding in its primary system is the nickel-based alloy 52M, which belongs to the 690 series of Ni-base alloys. Due to its higher Cr content, it offers superior SCC resistance compared to 600 series alloys [8~10]. Extensive research has been conducted on this type of DMWJ. Wang et al. [11] characterized the microstructure, microhardness, and composition variations in the fusion line interface region of A508/52M/316L DMWJs, finding significant differences in fracture toughness and crack propaga-

tion behavior at the weld/base metal interface compared to other joint regions. Choi et al. [12] investigated the effects of aging treatment on microhardness, composition, and intergranular Cr-carbide precipitation in low-alloy steel/Ni-base alloy DMWJ fusion line interfaces using TEM and three-dimensional atom probe (3D-APT). Hou et al. [13] studied the influence of transition zone microstructure on SCC resistance in Inconel 182/A533B low-alloy steel DMWJs. However, these studies lacked systematic investigation of all microstructural features across the entire joint.

Achieving localization of NPP design, construction, and raw materials is crucial for China' s nuclear energy industry to become independent from international constraints and promote sustainable energy development. Meanwhile, establishing appropriate integrity design and assessment methodologies for DMWJs is vital for safe NPP operation, as reliable safety evaluation enables scientific decisions regarding continued service, repair, or replacement when defects or cracks are detected. However, previous micro-characterizations of this joint were mostly limited to the weld width direction, neglecting potential structural and property variations along the thickness direction. This limitation hinders comprehensive understanding of the weldment' s overall microstructure, composition, and properties, potentially leading to discrepancies between research results on mechanical, electrochemical, and SCC susceptibility properties and actual service conditions.

Therefore, this work analyzed the microstructure, microhardness, distribution of main alloying elements, grain boundary character, and residual strain in the A508/52M/316L DMWJ for advanced PWR reactor pressure vessel safe-ends, and compared the microstructure and properties across different thickness locations of the entire weld joint, aiming to provide a basis for welding process optimization and service performance prediction and assessment.

The research object in this work is a domestically produced DMWJ for a PWR primary loop pipe safe-end. The reactor nozzle and safe-end materials are low-alloy steel A508 and 316L stainless steel (SS), respectively. The welding procedure involves depositing approximately 27 mm of nickel-based alloy 52M buttering layer on the A508 nozzle, followed by stress relief heat treatment. The nozzle and safe-end are then welded together using multiple passes with nickel-based alloy 52M filler metal. Although the buttering layer and butt weld use the same filler metal type, differences in filler batch and welding process result in slight variations in Cr and Ni content of the deposited metal, designated as 52Mb and 52Mw for distinction. To prevent direct contact between the corrosion-prone A508 and the PWR primary water environment, approximately 7 mm of nickel-based cladding is typically deposited on the inner wall surface near the port, while the remainder of the A508 inner wall is clad with 308 stainless steel. lists the main alloy element contents of each joint region. The macroscopic morphology of the joint cross-section is shown in [FIGURE:1]a. Due to the large sample size, it was sectioned into 8 pieces along the wall thickness direction, as shown in [FIGURE:1]b, where position 1 corresponds to the pipe inner wall and position

8 to the outer wall.

Different etching solutions were used for different regions. For the weld and cladding, two methods were employed: etching with a solution of 16 g $FeCl_3$ + 80 mL HCl + 2 mL HNO_3 + 11 mL H_2O, and electrolytic etching in 10% chromic acid solution (mass fraction) at 3 V for 20 s. For 316L SS, etching was performed using a solution of 5 g $CuSO_4$ + 25 mL HCl + 25 mL H_2O, or electrolytic etching in 10% ammonium persulfate solution for 2-3 min at 4 V. A508 was etched with 4% nital. The microstructure of the entire joint was examined using an Observer.Z1m optical microscope (OM). Local regions were studied using a JEM-2100F field emission transmission electron microscope (TEM). TEM samples were prepared as 3 mm diameter discs, mechanically ground to 50 μm, dimpled, and ion-milled. Microhardness measurements were conducted on an MHVD-1000AP microhardness tester with a 200 g load and 15 s dwell time. To reflect microhardness trends near the fusion line, adjacent indentations were spaced 150 μm apart near the fusion line and 500 μm apart in regions beyond 3 mm from the fusion line. The A508 HAZ and fusion line interface represent the most SCC-susceptible region of the weldment [11], requiring measurements at smaller intervals. Therefore, this region was measured with a 50 g load, 15 s dwell time, and 50 μm spacing between adjacent indentations. The distribution of main alloying elements near the fusion line interface was analyzed using energy-dispersive spectroscopy (EDS) on an XL30-FEG environmental scanning electron microscope (ESEM) with a scanning step of 0.42 μm and 2.0 s dwell time per point. Magnetic force microscopy (MFM) and scanning Kelvin probe force microscopy (SKPFM) tests were performed on a MultiMode IIID scanning probe microscopy system. The distribution of grain boundary types and residual strain near the fusion line was measured using electron backscatter diffraction (EBSD) on the ESEM. Samples were pre-ground with 2000-grit sandpaper, polished, and ultrasonically cleaned in alcohol for 30 min before measurement. An accelerating voltage of 25 kV was used, and data were analyzed using OIM software after acquisition. A threshold of 5° was set for calculating misorientation between adjacent points, with values below this threshold considered to be within the same grain.

2. Results and Discussion

2.1 Microstructure

2.1.1 52M Nickel-Based Alloy Weld [FIGURE:2] shows OM images of the 52M nickel-based alloy weld. As seen in [FIGURE:2]a, the butt weld microstructure consists of fully austenitic columnar grains that tend to grow perpendicular to the fusion boundary. The buttering alloy 52Mb differs from the butt weld 52Mw in that its grain structure grows horizontally, as shown in [FIGURE:2]b. The grain growth direction in the weld is determined by the solidification direction of the weld pool during welding, with obvious epitaxial growth between successive weld passes.

Observation of the entire weld pool microstructure revealed relatively uniform distribution along the weld depth direction, with no significant variations. [FIGURE:3] shows the macroscopic weld microstructure, where [FIGURE:3]a illustrates the sample macro-morphology at the middle position 4, clearly showing the characteristic vertical grain growth in the butt weld and horizontal growth in the buttering layer. In the central region of the weld joint, a layer of fine equiaxed grains appeared in the backing weld region (located at position 3, approximately 45 mm from the weld inner wall), as indicated by the arrow in [FIGURE:3]b. Researchers [14] have suggested that this equiaxed grain layer results from the accumulation of unmelted filler metal.

[FIGURE:4] shows the microstructure of the nickel-based alloy cladding near the A508 inner wall interface. The cladding consists of two layers of coarse columnar grains with large orientation differences between adjacent grains. Since both are nickel-based alloys, no complex microstructure due to composition variation appears in this region, and obvious epitaxial grain growth occurs between successive weld passes.

2.1.2 316L Stainless Steel Base Metal [FIGURE:5]a shows the microstructure of the 316L SS base metal, consisting of relatively uniform equiaxed annealed austenite grains with some twin structures. Numerous precipitate particles exist both in the HAZ near the weld and in the base metal away from the weld, with some large precipitate clusters distributed sporadically in the matrix, as shown in [FIGURE:5]b. Two types of precipitates are present: large particles several microns in size with irregular shapes, and smaller particles only a few hundred nanometers in size, with the latter being significantly less abundant than the former. EDS analysis of the precipitates revealed that the large and small particles contain 27.23% and 11.02% Cr, and 21.91% and 19.44% Mo (mass fraction), respectively—both higher than the Cr and Mo contents in the 316L matrix, while their Fe and Ni contents are correspondingly lower than in the base metal.

The morphology of large precipitates after etching with $CuSO_4$ and HCl solution is shown in [FIGURE:6]a, with the corresponding MFM image in [FIGURE:6]b. The results show that the large precipitate regions appear lighter than the matrix, indicating these precipitates are non-magnetic. The normal microstructure of 316L SS consists of austenite grains with intergranular δ-ferrite precipitates. Since ferrite is ferromagnetic at room temperature and would appear darker than non-magnetic austenite grains in MFM images, these precipitates can be identified as not being the normal δ-ferrite structure in 316L SS. SKPFM results in [FIGURE:6]c show that the large precipitates have a lower Volta potential than the surrounding austenite matrix. The potential profile along the dashed line in [FIGURE:6]d reveals a potential difference of up to 30 mV between the large precipitates and the matrix, indicating that these precipitates act as the anode in a micro-galvanic cell with the matrix under corrosive electrolyte conditions and are therefore more susceptible to corrosion.

Studies [15~18] have shown that when austenitic stainless steel is tempered between 600-1050°C, ferrite undergoes a eutectoid reaction $\delta \rightarrow \sigma + \gamma\_\{new\}$, forming tetragonal σ-phase. This reaction can proceed until all ferrite is transformed, with the σ-phase composition varying with heat treatment time and temperature but generally being richer in Cr and Mo and poorer in Ni than δ-ferrite. In austenitic stainless steels, σ-phase is a common intermetallic phase, and ferrite-stabilizing elements such as Cr, Mo, and Si promote its formation. Research [16] has also shown that σ-phase has a lower Volta potential than the γ-phase. Based on the composition, morphology, SKPFM data, and previous research results, the large precipitates are likely σ-phase. As a hard and brittle intermetallic phase, σ-phase is detrimental to fracture toughness. Considering that 316L is in direct contact with the harsh corrosive environment of PWR primary water, the extensive distribution of σ-phase in 316L SS will inevitably affect the safe-end' s corrosion resistance.

SEM and TEM images of the small precipitates are shown in

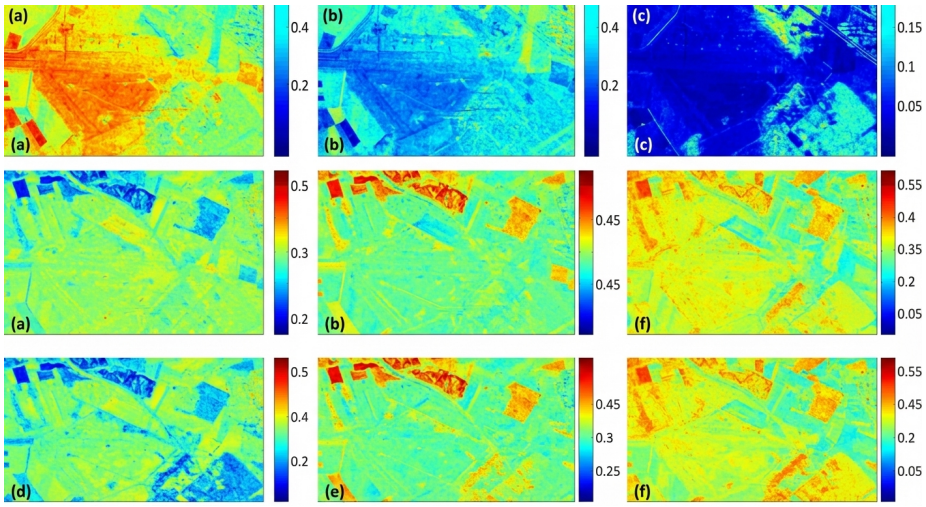

Figure 1: Figure 7

a and b, respectively, revealing significantly smaller particle sizes compared to the large precipitates. EDS analysis results in

c show no obvious Cr- or Mo-depleted zones around the small precipitates. Electron diffraction pattern indexing identified a bcc structure for these precipitates. Studies [18~22] have shown that Mo-containing austenitic stainless steels, ferritic stainless steels, and duplex steels may form a body-centered cubic precipitate called χ-phase when tempered between 600-900°C, with space group I43m and lattice constant of 0.892 nm. The χ-phase has a wide stoichiometric range, with a typical composition of $Fe_{36}Cr_{12}Mo_{10}$, though it usually contains other alloying elements such as Ti and Ni under actual conditions. Based on the electron

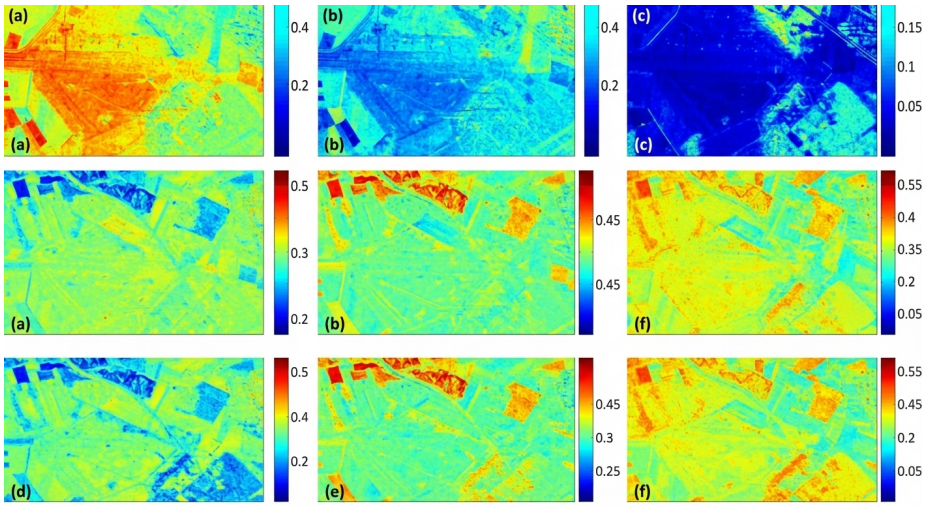

Figure 2: Figure 7

diffraction analysis and elemental composition, the small spherical precipitates are identified as χ-phase with a molecular composition of $(Fe, Ni)_{18}Cr_6Mo_5$. The χ-phase is also brittle and detrimental to both the corrosion resistance and mechanical properties of the safe-end.

[FIGURE:8] shows the OM image of the HAZ near the 316L SS fusion line. The grains adjacent to the fusion line exhibit some growth, as indicated by the arrows, and twin structures are reduced compared to the base metal. Otherwise, the microstructure shows no obvious difference from the base metal, and the distribution and morphology of precipitates remain unchanged despite the welding heat input [23].

2.1.3 A508 Low-Alloy Steel Base Metal The microstructure of A508 low-alloy steel is shown in [FIGURE:9]. The matrix consists of tempered bainite with some granular bainite within the feathery upper bainite structure. Both low-carbon regions ([FIGURE:9]a) and high-carbon regions ([FIGURE:9]b) exist, with significantly increased granular bainite content in the high-carbon regions.

[FIGURE:10] shows the microstructure of the A508 HAZ. The HAZ width is approximately 2-2.5 mm. [FIGURE:10]a illustrates the microstructural evolution from the 52Mb/A508 fusion boundary interface toward the A508 base metal, with the solid line marking the boundary between HAZ and base metal. The HAZ can be subdivided into four regions (I-IV) separated by dashed lines, corresponding to the fusion zone, coarse grain zone, fine grain zone, and tempered zone. Region I is white-appearing ferrite formed by decarburization adjacent to the fusion line. Region II corresponds to temperatures above the Ac_3 transformation temperature, where significant grain growth occurs and quenched

martensite forms upon cooling; depending on cooling rate and welding heat input, bainite may also form, creating a mixed martensite-bainite structure as shown by the arrows in [FIGURE:10]b. Region III corresponds to the Ac_1-Ac_3 temperature range where ferrite partially dissolves into austenite while pearlite, bainite, and sorbite fully transform to austenite; during cooling, the austenite transforms to fine martensite while the original ferrite remains unchanged but undergoes some grain growth, resulting in a ferrite + martensite mixed structure as shown in [FIGURE:10]c. Region IV exhibits obvious tempered microstructure characteristics, as shown in [FIGURE:10]d.

The microstructure of the HAZ on the A508 side adjacent to the inner wall cladding is similar to that near the buttering layer fusion line interface. However, in some regions, the area immediately adjacent to the fusion line consists of coarse lath martensite rather than white ferrite ([FIGURE:11]), while the regions farther from the fusion line show microstructures consistent with the fine grain and tempered zones of the HAZ.

2.1.4 316L/52Mw Fusion Boundary Interface [FIGURE:12] shows the microstructure near the 316L/52Mw fusion boundary interface. A special region composed of fine columnar crystals exists between the 316L SS and 52Mw weld. Research [24] has shown that heat flow and element diffusion during welding lead to the formation of complex microstructures at this interface that differ from both base and weld metals. Due to differences in melting temperatures between base and weld metals, an unmixed zone (UZ) commonly forms near the fusion line interface. This UZ is not continuously distributed along the entire fusion line, and its width varies at different thickness locations of the weld. The microstructure on the 52Mw weld side consists of transition-oriented austenite columnar grains that grow epitaxially from the 316L SS grains.

2.1.5 52Mb/A508 Fusion Boundary Interface [FIGURE:13] shows the microstructure near the 52Mb/A508 fusion boundary. A white-appearing transition zone (TZ) exists between 52Mb and A508 due to compositional transition, as shown in [FIGURE:13]a, indicating that the TZ is more etching-resistant than the adjacent base and weld metals under this etching system. Type-I and Type-II grain boundaries, characteristic of dissimilar metal welding, are also present in some regions, as shown in [FIGURE:13]b. Type-II boundaries are parallel to the fusion line interface, while Type-I boundaries connect the fusion line interface to Type-II boundaries. Studies [25~28] have shown that these boundaries form due to differences in crystal structure between weld and base metals and sharp compositional changes across the fusion line. Type-I boundaries grow epitaxially from base metal grain boundaries [25,29], and both Type-I and Type-II boundaries are high-angle grain boundaries with higher SCC susceptibility than the fusion line itself, providing preferential paths for crack initiation and propagation [13,30,31]. Research on 182-LAS DMWJs [32] has shown that this region exhibits the highest residual strain values. The presence of these special boundaries is one of the main reasons for the SCC susceptibility of DMWJs. However,

observation of the interface between the inner wall cladding and A508 ([FIGURE:11]) revealed no Type-I or Type-II boundaries, only the white-appearing TZ.

2.2 Microhardness Distribution

The microhardness distribution across the weldment is shown in [FIGURE:14]. The maximum microhardness appears in the A508 HAZ at approximately 320 HV. Three distinct regions of microhardness jumps correspond to the 316L/52Mw, 52Mw/52Mb, and 52Mb/A508 interfaces, with the most dramatic change occurring at the 52Mb/A508 interface. The 316L SS hardness ranges from 165-185 HV. From inner to outer wall, the HAZ hardness first increases then decreases, with peak values exceeding 255 HV at approximately 3 mm from the fusion line. Austenitic stainless steel has a high coefficient of thermal expansion and low thermal conductivity, and its thermal property differences from the 52M nickel-based alloy can generate significant residual stress and deformation in the weld HAZ, leading to increased microhardness and crack susceptibility.

The weld metal shows relatively uniform hardness, with the butt weld being slightly harder than the buttering layer overall, likely due to post-weld stress relief treatment of the buttering layer and the unconstrained welding conditions. The regions on the weld side of the 316L/52Mw and 52Mb/A508 interfaces exhibit the lowest hardness in the entire weld, possibly due to element migration near the interface reducing Cr and Ni contents and weakening solid solution strengthening [33].

The microhardness distribution in the A508 HAZ is shown in [FIGURE:14]d. Moving from the fusion line toward the A508 base metal, the microhardness increases sharply then gradually decreases, with the highest hardness occurring approximately 600 μm from the fusion line, corresponding to the mixed martensite-bainite structure region in the coarse grain zone ([FIGURE:10]b). In the transition region between HAZ and base metal, the microhardness is lower than in both the HAZ and base metal, creating a locally softened zone. This softening results from the welding heat flow tempering this region at high temperature, promoting carbon migration and softening the tempered bainite structure in the base metal [11]. However, the microhardness of the A508 HAZ adjacent to the inner wall cladding is lower than that near the 52Mb buttering layer, possibly due to different welding processes for the cladding and buttering layers.

Comparison of microhardness data from inner wall, outer wall, and middle sections reveals similar distributions along the weld thickness direction. The average microhardness of the backing weld sample at position 5 is higher than that of samples at inner wall position 1 and outer wall position 8. This is because regions closer to the backing weld experience more thermal cycles, resulting in greater effects on hardness.

2.3 Distribution of Main Alloying Elements Near Fusion Lines

2.3.1 316L/52Mw Fusion Boundary [FIGURE:15] shows the distribution of main alloying elements Fe, Cr, Ni, and Mo near the 316L/52Mw fusion boundary at weld middle position 4, with [FIGURE:15]a and b corresponding to regions without and with an unmixed zone (UZ), respectively. The results show significant concentration changes near the interface caused by element migration driven by concentration gradients between base and weld metals during welding. However, the elemental mass fractions in the UZ differ from those in both the base metal and filler metal, likely due to incomplete dilution of partially melted base metal resulting from melting temperature differences [34]. The element composition in the transition zone (TZ) on the 52Mw side shows gradient variation, and the TZ width is larger when a UZ is present. Studies [28,29] have shown that element migration at the interface promotes the formation of complex microstructures in the 316L/52Mw interface region, affecting the mechanical properties and SCC resistance of the weld joint. Comparison of inner wall, middle, and outer wall results shows similar compositional transition trends near the 316L/51Mw interface at different thickness locations.

2.3.2 52Mb/A508 Fusion Boundary [FIGURE:16] shows the distribution of main alloying elements Fe, Cr, and Ni near the 52Mb/A508 fusion boundary at weld middle position 4, with [FIGURE:16]a and b corresponding to regions without and with Type-I and Type-II boundaries, respectively. As shown in [FIGURE:16]a, Fe content gradually increases while Ni and Cr contents gradually decrease within the TZ on the 52Mb side; composition changes are less obvious on the A508 side. In regions with Type-I and Type-II boundaries, Fe content decreases slightly while Cr and Ni contents increase somewhat between the Type-II boundary and fusion line. The element distribution near the fusion line interface between the inner wall cladding and A508 is similar to that in regions without Type-I and Type-II boundaries. Again, comparison of inner wall, middle, and outer wall results shows similar compositional transition trends near the 52Mb/A508 interface at different thickness locations.

2.4 Grain Boundary Character Distribution Near Fusion Lines

2.4.1 316L/52Mw Fusion Boundary EBSD images of grain boundary character distribution near the 316L/52Mw fusion boundary are shown in [FIGURE:17], with grain boundary character distribution (GBCD) statistics presented in [FIGURE:18]. The results indicate that 316L SS is dominated by high-angle grain boundaries and coincidence site lattice (CSL) boundaries, with a small proportion of low-angle grain boundaries. Moving from the fusion line toward the base metal, the fraction of CSL boundaries gradually increases, exceeding that of high-angle grain boundaries at 7 mm from the fusion line, with most twin boundaries identified as CSL boundaries. Statistical results show that CSL boundaries are predominantly $ $3 boundaries, with negligible fractions of other CSL types. Research [35~38] has demonstrated that $ $3 boundaries in

CSL boundaries exhibit excellent SCC resistance. The fraction of CSL boundaries in the 316L HAZ is significantly lower than in the base metal, indicating that the welding process adversely affects SCC resistance. The 52Mw weld metal is dominated by high-angle grain boundaries with relatively low contents of low-angle and CSL boundaries. Numerous small "grains" appear in some weld regions ([FIGURE:17]a6, b7, c5), with most of their boundaries identified as CSL boundaries. The distribution trends are consistent through the weld thickness, with similar proportions of the three boundary types.

2.4.2 52Mb/A508 Fusion Boundary The grain boundary character distribution on both sides of the 52Mb/A508 fusion boundary is represented by the outer wall (position 7) results shown in [FIGURE:19], with GBCD statistics for inner wall (position 1) and outer wall presented in [FIGURE:20]. Both sides of this fusion boundary are dominated by high-angle grain boundaries with small amounts of low-angle grain boundaries and almost no CSL boundaries. Moving from the fusion line toward the A508 matrix, grain size first decreases then increases. Comparison of inner and outer wall data shows consistent trends in grain boundary character variation near this interface through the weld thickness direction.

2.5 Residual Strain Distribution Near Fusion Lines

Kernel average misorientation (KAM) values quantitatively reflect the degree of strain hardening. [FIGURE:21] shows the residual strain distribution near the fusion line interface of the inner wall (position 1), with KAM value statistics presented in [FIGURE:22].

Near the 316L/52Mw fusion line, KAM values increase then decrease moving from the fusion line into the 316L SS matrix. This occurs because welding heat flow generates localized high temperatures and rapid heating/cooling rates near the fusion line, producing maximum residual strain. As distance from the fusion line increases, peak temperature and heating/cooling rates decrease, resulting in gradually reduced residual strain [27,39]. Residual strain values in the backing weld region are higher than in the inner and outer walls due to the greater number of thermal cycles experienced [40]. Weld metal KAM values are lower than those in the base metal HAZ, but inner and outer wall KAM values first decrease, then increase, then decrease again moving from the fusion line into the weld, while the backing weld does not show this trend. This difference may be related to the different positions of the scanned regions within the weld: the location 7 mm from the fusion line in the backing weld is near the 52Mw/52Mb fusion line, while the corresponding locations in the inner and outer walls are in the middle of the weld pool.

Near the 52Mb/A508 fusion line, KAM values show smaller fluctuations and much lower average values than near the 316L/52Mw fusion line, because the buttering layer welding was performed without constraint, resulting in less welding deformation. Inner and outer wall data show consistent trends, with slightly

higher KAM values at the outer wall.

3. Conclusions

1. Both the butt weld and buttering layer consist of coarse columnar austenitic grains. Transition zones (TZ) of certain width exist near fusion lines. A discontinuous unmixed zone (UZ) composed of small columnar crystals was observed at the 316L/52Mw interface, while discontinuous Type-I and Type-II grain boundaries appeared on the A508 side. Significant composition fluctuations occurred in the UZ, Type-I, and Type-II boundary regions.

2. The A508 base metal matrix consists of tempered bainite, with a complex HAZ microstructure comprising four regions: fusion zone, coarse grain zone, fine grain zone, and tempered zone. The 316L base metal consists of austenite with numerous granular precipitates and some twin structures, with no obvious HAZ microstructure.

3. The maximum microhardness of the weld joint appears in the A508 HAZ. Microhardness jumps occur near the three fusion line interfaces. The microhardness in both the 316L SS and A508 HAZs first increases then decreases with distance from the fusion line.

References

[1] Han E-H, Wang J Q, Wu X Q, Ke W. Acta Metall Sin, 2010; 46: 1379
[2] Joseph A, Rai S K, Jayakumar T, Murugan N. Int J Pressure Vessels Piping, 2006; 82: 700
[3] Seifert H P, Ritter S, Shoji T. J Nucl Mater, 2008; 378: 197
[4] Wang H T, Wang G Z, Xuan F Z, Tu S T. Eng Failure Analysis, 2013; 28: 134
[5] Peng Q J, Xue H, Hou J, Sakaguchi K, Takeda Y, Kuniya J, Shoji T. Corros Sci, 2011; 53: 4309
[6] Hou J, Peng Q J, Kuniya J, Shoji T, Wang J Q, Han E H, Ke W. J Mater Sci, 2010; 397: 109
[7] Li G F, Congleton J. Corros Sci, 2000; 42: 1005
[8] Meng F J, Wang J Q, Han E-H, Shoji T, Ke W. Acta Metall Sin, 2011; 47: 839
[9] Bowerman B S, Czajkowski C J, Roberts T C, Neal C. Mater Charact, 1999; 43: 347
[10] Li G F, Li G J, Fang K W, Peng J, Yang W. Acta Metall Sin, 2011; 47: 797
[11] Wang H T, Wang G Z, Xuan F Z, Liu F Z, Tu S T. Mater Sci Eng, 2013; A568: 108
[12] Choi K J, Kim J J, Lee B H, Bahn C B, Kim J H, J. Nucl Mater, 2013; 441: 493
[13] Hou J, Peng Q J, Lu Z P, Shoji T, Wang J Q, Han E H, Ke W. Corros Sci,

2010; 52: 3949
[14] Hanninen H, Brederholm A, Toivonen A. 15th International Conference on Environmental Degradation of Materials in Nuclear Power Systems-Water Reactors, Colorado Springs: TMS, 2011: 197
[15] Sathirathinda N, Gubner R, Pan J, Kivisakk U. Electrochem Solid-State Lett, 2008; 11: C41
[16] Kasper J S. Acta Metall, 1954; 2: 456
[17] Michalska J, Sozanska M. Mater Charact, 2006; 56: 355
[18] Popov A A, Bannikova A S, Belikov S V. Phys Met Metall, 2009; 108: 586
[19] Chun E J, Baba H, Nishimoto K, Saida K. Mater Charact, 2013; 86: 152
[20] Escriba D M, Materna-Morris E, Plaut R L, Padilha A F. Mater Charact, 2009; 60: 1214
[21] Martin D S, Rivera Diaz del Castillo P E J, Peekstok E van del Zwaag S. Mater Charact, 2007; 58: 455
[22] Lai J K L, Meshukat M. Met Sci, 1978; 9: 416
[23] Falata L, Svoboda M, Výrostkova A, Petryshynets I, Sopko M. Mater Charact, 2012; 72: 15
[24] Naffakh H, Shamanian M, Ashrafizadeh F, J. Mater Process Technol, 2009; 209: 3628
[25] Nelson T W, Lippold J C, Mills M J. Sci Technol Weld Joining, 1998; 77: 249
[26] Rowe M D, Nelson T W, Lippold J C. Sci Technol Weld Joining, 1999; 78: 31
[27] Srinivasan P B, Muthupandi V, Dietzel W, Sivan V. Mater Des, 2006; 27: 182
[28] Hou J, Peng Q J, Shoji T, Wang J Q, Ke W, Han E-H. Acta Metall Sin, 2010; 46: 1258
[29] Asami K, Sakai T. Trans Iron Steel Inst Jpn, 1981; 21: B269
[30] Nelson T W, Lippold J C, Mills M J. Sci Technol Weld Joining, 1999; 78: 329
[31] Nelson T W, Lippold J C, Mills M.J. Sci Technol Weld Joining, 2000; 79: 267
[32] Hou J, Peng Q J, Takeda Y, Kuniya J, Shoji T, Wang J Q, Han E-H, Ke W. J Mater Sci, 2010; 45: 5332
[33] Wang H T. PhD Dissertation, East China University of Science and Technology, Shanghai, 2013
[34] Naffakh H, Shamanian M, Ashrafizadeh F. J Mater Process Technol, 2009; 209: 3628
[35] Gertsman V Y, Tangri K, Valiev R Z. Acta Metall Mater, 1994; 42: 1785
[36] Gertsman V.Y, Bruemmer S M. Acta Mater, 2001; 49: 1589
[37] Lehockey E M, Brennenstuhl A M, Thompson I. Corros Sci, 2004; 46: 2383
[38] Pan Y, Adams B L, Olson T, Panayotou N. Acta Mater, 1996; 44: 4685
[39] Lee H T, Wu J L. Corros Sci, 2009; 51: 733
[40] Qiao D, Zhang W, Pan T Y, Crooker P, David S, Feng Z. Sci Technol Weld Joining, 2013; 92: 624

ChinaRxiv 中X

Source: ChinaXiv —Machine translation. Verify with original.